by the *Österreichische Nationalbank, Jubiläumsfonds-Projekt Nummer 6876.*

For the progress of the work, the skilful support by our colleagues at the ESO duty stations Garching, La Silla and Santiago and at the *Friedrich-Schiller-Universität,* Jena, was of great help in all phases. Special thanks go to the staff of the machine shop of the Physics Department of the *Friedrich-Schiller-Universität* who actually manufactured the majority of the mechanical parts from raw materials, and to the *Astro-Taller* on La Silla.

References

E. Dietzsch and H.-G. Reimann, 1998; TIMMI2: A Combined Astronomical MIR Camera, Spectrometer and Polarimeter for ESO; Proceedings SPIE Vol. **3482,** pp. 151–160.

A.D. Estrada, G. Doingo, J.D. Garnett, A.W. Hoffman, N.A. Lum, P.J. Love, S.L. Solomon, J.E. Venzon, G.R. Chapman, C. McCreight, M. McKelvey, R. McMuray, J. Estrada, S. Zins, R. McHugh, and R. Johnson, 1998; Si: As IBC IR focal plane arrays for ground-based and space-based astronomy; Proceedings of SPIE conference 3354 Infrared Astronomical Instrumentation, Kona 1998, pp. 99–108.

S. Guisard, U. Weilenmann, A. van Dijsseldonk, H.U. Käufl, and J. Roucher, 1997; Image Quality of the 3.6m Telescope (part VI): Now Diffraction Limited at 10 Microns at the f/35 Focus; *The Messenger* **90**, 9–11.

H.U. Käufl, P. Bouchet, A. van Dijsseldonk and U. Weilenmann, 1991; A Sky-Noise Measurement and its Implication for Ground-Based Infrared Astronomy in the 10-µm Atmospheric Window; *Experimental Astronomy* **2**,115–122.

H.U. Käufl, R. Jouan, P.O. Lagage, P. Masse, P. Mestreau and A. Tarrius, 1992; TIMMI at the 3.6m Telescope; *The Messenger* **70**, 67–70.

H.U. Käufl, 1993; Ground-Based Astronomy in the 10 and 20µm Atmospheric Windows at ESO – Scientific Potential at Present and in the Future; *The Messenger* **73**, 8–12.

H.U. Käufl and B. Delabre, 1994; Improved Design and Prototyping for a 10/20µm Camera/Spectrometer for ESO's VLT, in proc. of *Instrumentation in Astronomy VIII;* SPIE Vol 2198, p. 1036–1047.

H.U. Käufl, R. Jouan, P.O. Lagage, P. Masse, P. Mestreau, A. Tarrius, 1994a; TIMMI, ESO's new 10µm Camera/Spectrometer; *Infrared Phys. Technol.* **35**, 203–210.

H.U. Käufl, 1994b; N-Band Long-Slit Grism Spectroscopy with TIMMI at the 3.6m Telescope; *The Messenger* **78**, 4–7.

P.O. Lagage, R. Jouan, P. Masse, P. Mestreau, A. Tarrius, H.U. Käufl; 1993, TIMMI: a 10 µm Camera for the ESO 3.6m telescope; in proc. SPIE vol. 1946, p. 655–666, *Infrared Detectors and Instrumentation,* A.M. Fowler (ed.).

H.U. Käufl, 1995a; Acquisition, cleaning and calibrating of ground based thermal IR data; in proc. of the ESO/ST-ECF workshop on *Calibrating and understanding NST and ESO instruments,* ESO, ed. P. Benvenuti p. 99–104.

H.U. Käufl, 1995b; Observing extended objects with chopping restrictions on 8m class telescopes in the thermal infrared; in proc. of the ESO/ST-ECF workshop on *Calibrating and understanding HST and ESO instruments,* ESO, ed. P. Benvenuti p. 159–164.

C. Lucas, P. Pantiguy, D. Alloin, C. Cesarsky, P.O. Lagage, H.U. Käufl, J.L. Monin, 1994; New 8-13µm Si:Ga/DRO Hybrid Arrays for Very Large Telescopes; Proc. of *Infrared astronomy with arrays: the next generation*, p. 425–428, ed. I. McLean, Kluwer.

A. Moorwood and A. van Dijsseldonk, 1985; New Infrared Photometer and F/35 Chopping Secondary at the 3.6m Telescope; *The Messenger* **39,** p. 1.

H.G. Reimann, U. Weinert and S. Wagner, 1998; "TIMMI2, a new IR-Multimode Instrument for ESO", Proc. SPIE Conf. **3354**, p. 865. (See also http://cdsads.u-strasb.fr/cgi-bin/nph-bib_query?bibcode=1998SPIE.3354..865R&db_key=)

H. Relke, M. Sperl, J. Hron, H.U. Käufl, H. Linz, H.G. Reimann, R. Wagner: 2000. Proc. SPIE Vol. 4009, p. 440–448, Advanced Telescope and Instrumentation Control Software, Hilton Lewis, Ed.

B. Stecklum, H.U. Käufl, A. Richichi, 1999; The lunar occultation of CW Leo – a great finale for TIMMI, 1999 *The Messenger* **95**, 25–27.

Email address: hukaufl@eso.org

Exploring the Lyman Forest at *z* = 2 with UVES

S. CRISTIANI, S. D'ODORICO, T.-S. KIM, ESO

1. The Signature of Neutral HI in the High-Redshift Universe

The Lyman-α resonance line of neutral hydrogen provides a sensitive probe to study the cosmological distribution of the baryonic matter and the conditions in the intergalactic medium (IGM) over a wide range of redshifts, up to $z \sim 6$. Observations of the "forest" of Lyman-α absorptions along the lines of sight to quasars, the most luminous objects known, reveal a wealth of structures, ranging from fluctuations of the diffuse IGM to the interstellar medium in protogalactic objects. The properties of the Lyman-α forest at different redshifts constrain the cosmological parameters, such as the density of baryons and the density parameter Ω, and are the key to issues like the formation of galaxies and large-scale structure, the origin and properties of the ionising radiation background. In particular, it was early recognised by Gunn & Peterson (1965) that, to avoid producing a very large HI opacity at wavelengths just below that of the quasar's Lyman-α emission line, a strong photoionisation by the metagalactic UV background is necessary, which at high redshift is produced by the first generation of stars, which also enrich the IGM with metals (also observed in the form of absorptions).

Unlike most of the other astronomical objects, Lyman-α absorbing "clouds"

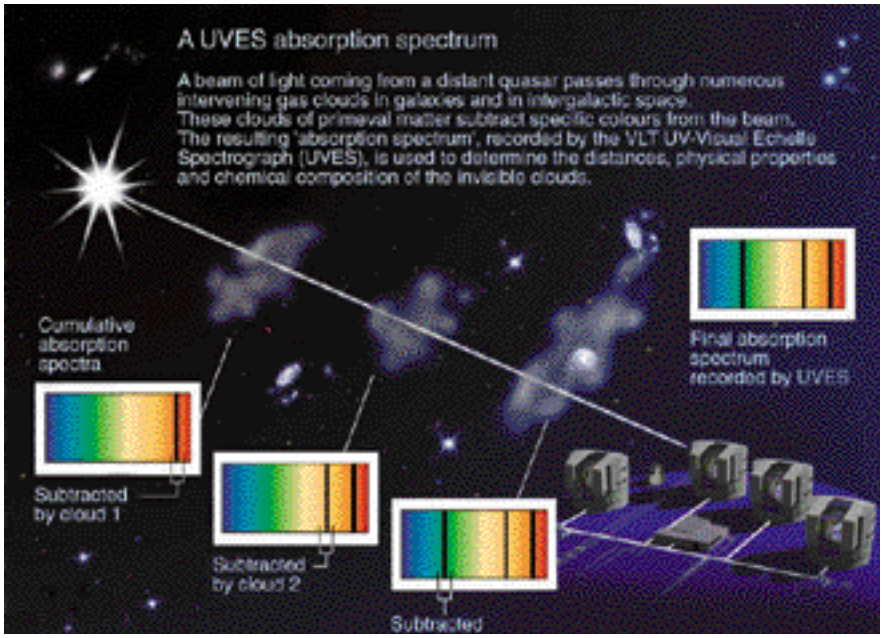

Figure 1: An artistic view (thanks to Ed Janssen) of how absorbing "clouds" distributed in the Universe leave their imprint in the spectrum of a distant, background quasar, which acts as a light beacon.

were first discovered at great distances ($z \gtrsim 2$) due to cosmological redshift and the near-UV atmospheric absorption. Only in relatively recent times and with the advent of the Hubble Space Telescope (HST) has it been possible to gain a limited (in sensitivity and resolution) access to the ultraviolet and study nearby examples. The epoch corresponding to redshifts between 1.5 and 2.5 is one of the most interesting, characterised by an intense universal star formation, though one of the most difficult to study because the "signatures" of luminous matter at these reshifts (both stars and emitting gas) fall mainly in the less accessible IR region. The key resonance absorption lines like Lyman-α lie at these redshifts in the UV region where, before UVES, no efficient high-resolution spectrograph was in operation at very large telescopes.

2. A First Look at the IGM at z = 2 with the New Echelle Spectrograph at the VLT, UVES

UVES (Dekker et al. 2000) is the two-arm echelle spectrograph, mounted on one of the Nasmyth platforms of the Kueyen telescope (UT2) of the VLT. In the instrument design phase it was decided to go for a two-arm configuration (UV-Blue and Visual-Red channels, to be operated in parallel with a dichroic beam splitter) to optimise the efficiency especially in the extreme UV (close to the atmospheric cut-off) and in the Near-Infrared (where IR array-based instruments start to become competitive with CCD-based ones). CCD devices, gratings and coatings of optical materials for a variety of reasons cannot be manufactured with a flat, maximised efficiency curve over the 300–1100 nm range. By splitting the range in two, remarkable gains can be achieved at the extreme wavelengths. The current efficiency curve of UVES is shown in Figure 2. The efficiencies below 400 nm and above 800 nm are considerably higher than in the powerful echelle spectrograph HIRES which has been successfully in operation for a few years now at Keck.

This advantage immediately offers the possibility of obtaining new results. The observations of the Lyman alpha forest in the spectra of quasars at z = 1.5–2 is a good example of the pay-off of the higher UV efficiency. Already during commissioning and science verification, QSOs at redshift around 2 were extensively observed and the data are now available from the ESO archive. The analysis on the forest (Kim, Cristiani & D'Odorico 2000) gives the first detailed information on the IGM in this redshift range.

To illustrate the extraordinary possibilities offered by UVES in terms of sensitivity and resolution, a small portion of

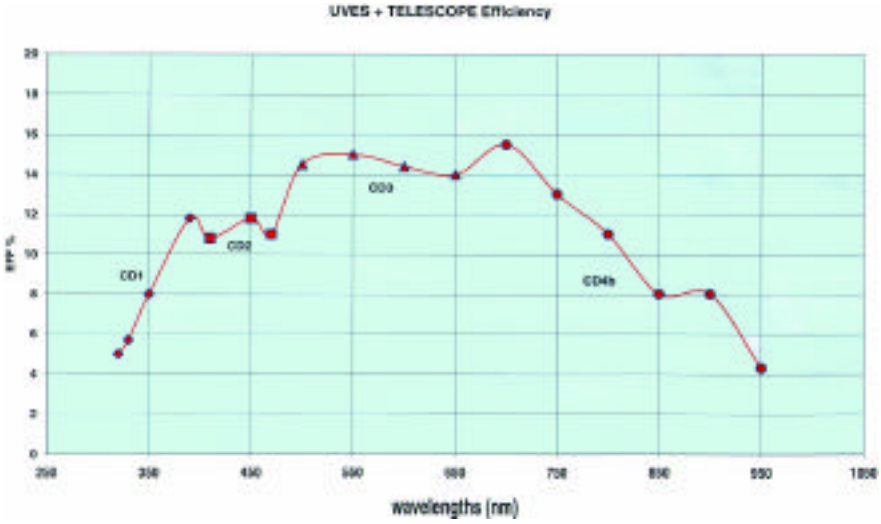

Figure 2: The overall detection efficiency of UVES including the three reflections in the telescope. No atmospheric absorption and no slit losses. The values have been derived from observations of spectrophotometric standards. The overall range is covered by two UVES exposures in dichroic mode. The different symbols correspond to the spectral ranges covered by the 4 different cross-disperser gratings (CD). The Blue arm of the spectrograph was used till 470 nm. Status as of November 2000, after the installation of the final CD4.

the spectrum of the QSO HE 0515-44 is shown in Figure 3, in the range 310–326 nm.

The data have been reduced with the UVES pipeline (Ballester et al. 2000) and analysed with the package VPFIT (Carswell et al.: http://www.ast.cam.ac.uk/~rfc/vpfit.html). Voigt profiles are fitted to the absorption lines (isolated and in groups) to derive the redshifts z, the Doppler parameters b, and the column densities N.

3. The Evolutionary Properties of the Lyman Forest

3.1 The opacity of the IGM and the number density of Lyman-α lines

Figure 4 shows the Lyman-forest normalised spectra of two QSOs: the high-z Q0000-263 with an emission redshift z_{em} = 4.127 and the HDF-S QSO, J2233-606, with an emission redshift z_{em} = 2.238. The resolution of the two echelle spectra has been degraded to cover the full range between the Lyman-α and Lyman-β emissions. It is impressive to see how fast the number of absorptions (and the average opacity) increases with increasing redshift. The HI opacity, τ_{HI}, can be defined as $f_\lambda = f_c \exp^{-\tau_{HI(\lambda)}}$, where f_λ is the observed flux at a wavelength λ and f_c is the unabsorbed continuum level. We can compute then the effective opacity τ_{eff} as $\exp^{-\tau_{eff}} = < \exp^{-\tau} >$, where $< >$ indicates the mean value averaged over λ.

The new UVES results, together with data from the literature, show that the evolution of the effective opacity follows pretty well an exponential law from z =

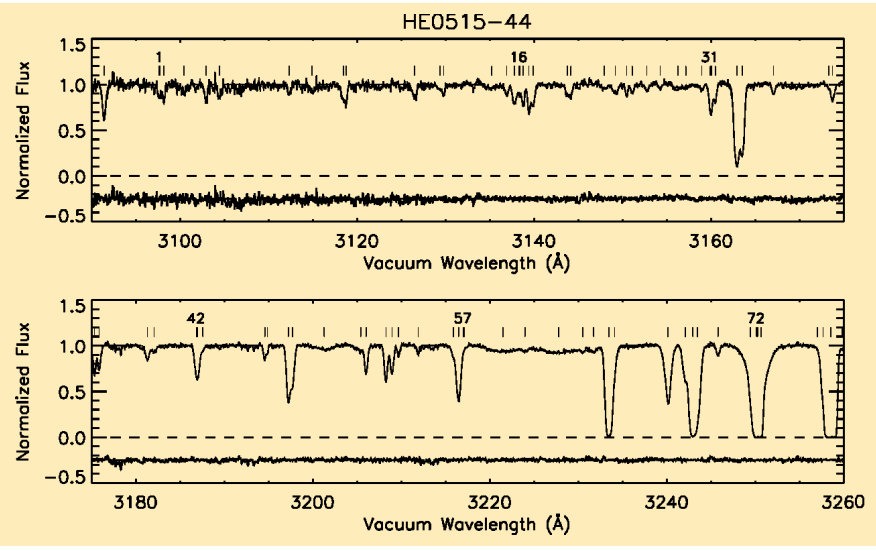

Figure 3: The spectrum of HE0515-44 superposed with the Voigt profile fitted spectrum. The residuals (the differences between the observed and the fitted flux) shown in the bottom part of each panel are shifted by –0.25.

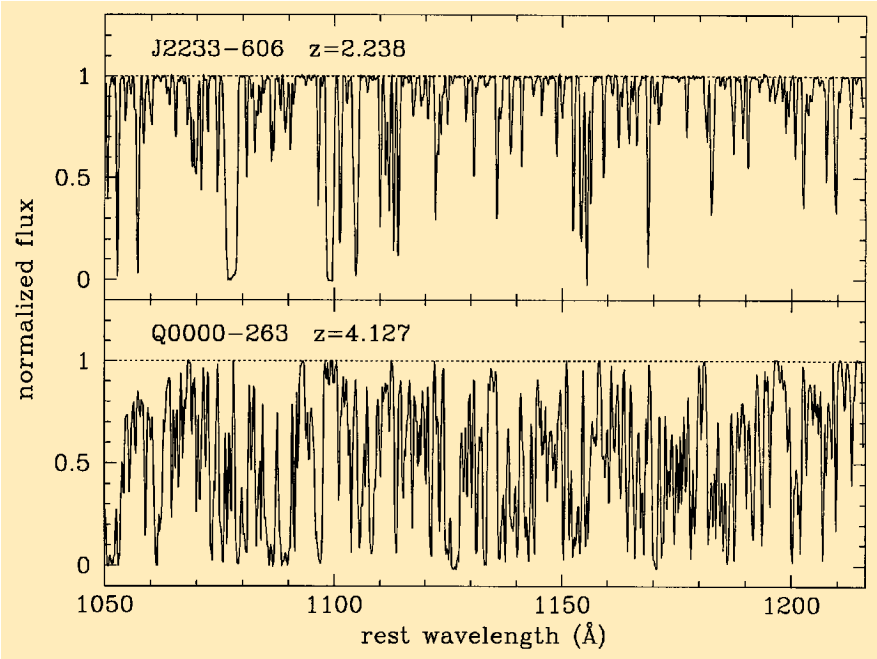

Figure 4: Comparison between the Lyman-α forest of two QSOs: J2233-606 with an z_{em} = 2.238 and Q0000-263 with an z_{em} = 4.127. The exponential increase of the number of lines with increasing redshift is apparent.

1.6 up to z ~ 5: $\bar{\tau}_{eff}(z)$ = 0.0034 ± 0.0009 $(1+z)^{3.35\pm0.17}$.

The number density of lines per unit redshift is defined as $N(z) = N_0(1+z)^{\gamma}$, where N_0 is the local comoving number density of the forest. For a non-evolving population, γ = 1 and 0.5 for q_0 = 0 and 0.5, respectively. Figure 5 shows the number density evolution of the Lyman-α forest in the interval $N_{HI} = 10^{13.64-16}$ cm^{-2}. This range has been chosen to allow a comparison with the HST sample at z < 1.5 of Weymann et al. (1998), for which a threshold in equivalent width of 0.24 Å was adopted. The long-dashed line is the maximum-likelihood fit to the UVES and the HIRES data at z > 1.5: $dN/dz = (6.7 \pm 3.8)(1+z)^{2.38\pm0.15}$. Interestingly, the HST data point at $\langle z \rangle$ = 1.6 (the open triangle at the boundary of the shaded area), which has been measured in the line-of-sight to the QSO UM 18 and suggested to be an outlier, is now in excellent agreement with the extrapolated fit from higher z. The UVES observations imply that the turn-off in the evolution does occur at z ~ 1.2, not at z ~ 1.7 as previously suggested. Down to z ~ 1.5, the number density of the forest evolves as at higher z.

The evolution of the N(z) is governed by two main factors: the Hubble expansion and the metagalactic UV background. At high redshift, the expansion, which tends to increase the ionisation of the matter (the rate of recombination is quadratically dependent on the density), and the UV background, increasing or non-decreasing with decreasing redshift, work in the same direction and cause a steep evolution of the number of lines with z. At low redshift, the UV background starts to decrease with decreasing redshift, due to the reduced number of ionising sources, and this effect counteracts the Hubble expansion. As a result, the evolution of the number of lines slows down. Up to date, numerical simulations have been remarkably successful in reproducing the observed evolution (see, for example Davé et al. 2000, Machaceck et al. 2000), leaving little doubt about the general interpretation of the phenomenon. However, the same simulations predicted the break in the dN/dz power law at a redshift z ~ 1.8 that now appears too high. This suggests that the UV background implemented in the simulations is not the correct one: it was thought that at low redshift QSOs are the main source of ionising photons, and, since their space density drops below z ~ 2, so does the UV background. However, galaxies can produce a conspicuous ionising flux too, perhaps more significant than it was thought, as shown by recent measurements by Steidel et al. (2000). The galaxy contribution, then, can keep the UV background relatively high until at z ~ 1 the global star formation rate in the Universe quickly decreases, determining the qualitative change in the number density of lines.

3.2 The temperature of the IGM

If the Lyman-α forest is in thermal equilibrium with the metagalactic UV background, the line width of the absorption lines, described by the b parameter of the Voigt profile, is directly related to the gas temperature of the absorbing medium determined by the balance between adiabatic cooling and photoheating: $b = \sqrt{2kT/m_{ion}}$. In practice, additional sources of broadening exist, such as the differential Hubble flow across the absorbers, peculiar motions, Jeans smoothing. However, a lower limit to the line widths exists, set by the temperature of the gas. Hence we can measure this cutoff and get the temperature of the IGM. The situation is slightly more complex because for a photoionised gas, there is a temperature-density relation, i.e. the equation of state: $T = T_0(1+\delta_b)^{\gamma_T - 1}$, where T is the gas temperature, T_0 is the gas temperature at the mean gas density, δ_b *is* the

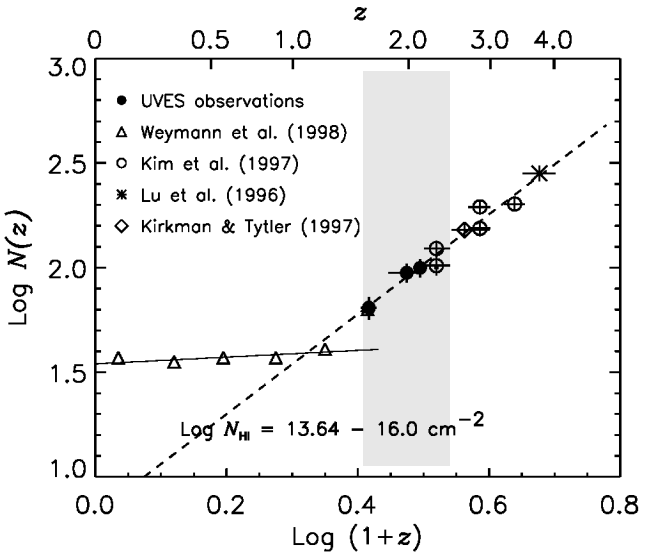

Figure 5: The number density evolution of the Lyα forest. The column density range $N_{HI} = 10^{13.64-16}$ cm^{-2} has been chosen to allow the comparison with the HST data of Weymann et al. (1998), which are shown as open triangles. The filled symbols are derived from HE 0515–44 at $\langle z \rangle$ = 1.61, from J2233–606 at $\langle z \rangle$ = 1.98 and from HE 2217–2818 at $\langle z \rangle$ = 2.13. The open circles, the star, and the diamond are taken from the HIRES data at similar resolutions by Kim et al. (1997), Lu et al. (1996), and Kirkman & Tytler (1997), respectively. The horizontal error bars represent the z interval over which the number density was estimated. The vertical error bars represent the Poisson 1σ error. The shaded area is the z range where UVES is extremely sensitive. The long-dashed line is the maximum likelihood fit to the UVES and the HIRES data at z > 1.5. The UVES observations indicate that the slope of the number density evolution of the Lyα forest at z > 2.4 continues at least down to z ~ 1.5 and that a change occurs at z ~ 1.2.

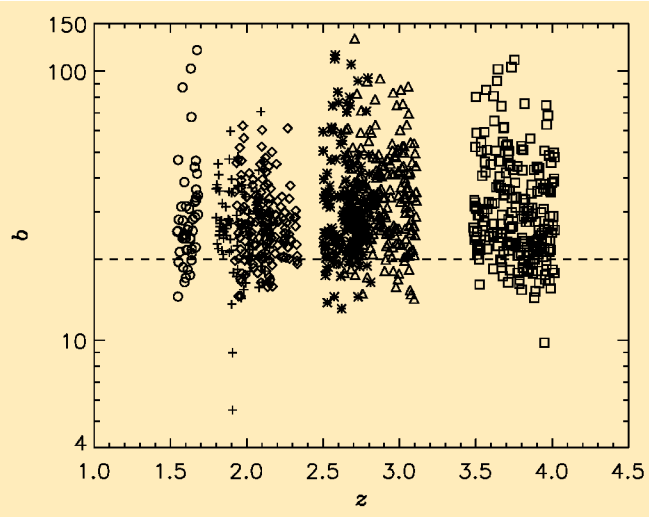

Figure 6: The b distribution of the Lyα forest as a function of z. The horizontal dashed line indicates a 20 km/sec b_c value. The circles, the pluses, the diamonds, the stars, the triangles and the squares are from HE0515–44, J2233–606, HE2217–2818, HS1946+7658, Q0302–003 and Q0000–263, respectively. There is an indication of increasing b_c with decreasing z at z ~ 3.7. At lower z, b_c is not clearly defined.

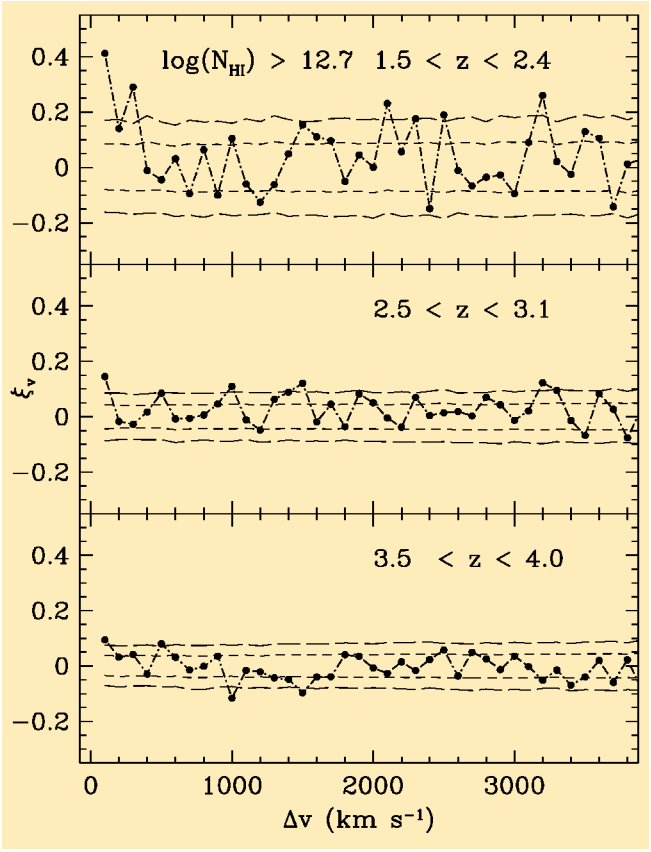

Figure 7: Evolution of the two-point correlation function with redshift for Lyα lines with column densities above $N_{HI} = 10^{12.7}$ cm^{-2}. The short-dashed and long-dashed lines represent the 1σ and 2σ confidence limits for a Poissonian process.

baryon overdensity, $(\rho_b - \bar{\rho}_b)/\bar{\rho}_b$ and γ_T is a constant which depends on the ionisation history (Hui & Gnedin, 1997). The equation of state translates into a lower cut-off $b_c(N_{HI})$ in the N_{HI}–b distribution.

In Figure 6, the *b* distribution of the Lyα forest as a function of *z* is shown. The cut-off Doppler (*b*) parameter seems to be approximately constant with $b_c \sim 18$ km s^{-1} at $1.5 < z < 4$, corresponding to a reference temperature of $2 \cdot 10^4$ K. Two possible features are observed: a systematic increase of the *b* values from $z \sim 4$ to $z \sim 3.5$ – due to the HeII reionisation? (Schaye et al. 2000) and a region of higher-than-average Doppler widths at $2.2 < z < 2.4$ that will be further discussed in the last subsection.

3.3 The clustering properties of the Lyman forest

The Lyman-α forest contains information on the large-scale distribution of the matter and the simplest way to study it is to compute the two-point velocity correlation function, ξ(Δ*v*). The correlation function compares the observed number of pairs (N_{obs}) and the expected number of pairs (N_{exp}) from a random distribution in a given velocity bin (Δ*v*): $\xi(\Delta v) = N_{obs}(\Delta v)/N_{exp}(\Delta v) - 1$, where $\Delta v = c\,(z_2 - z_1)/[1 + (z_2 + z_1)/2]$, z_1 and z_2 are the redshifts of two lines and *c* is the speed of light (Cristiani et al. 1997; Kim et al. 1997).

Studies of the correlation function of the Lyα forest have generally led to conflicting results even at similar *z*. Some studies find a lack of clustering (Sargent et al. 1980 at $1.7 < z < 3.3$; Rauch et al. 1992 at $z \sim 3$; Williger et al. 1994 at $z \sim 4$), while others find clustering at scales $\Delta v \leq 350$ km s^{-1} (Cristiani et al. 1995, 1997 at $z \sim 3$; Hu et al. 1995 at $z \sim 2.8$; Kulkarni et al. 1996 at $z \sim 1.9$; Lu et al. 1996 at $z \sim 3.7$). Figure 7 shows the velocity correlation strength at $\Delta v < 4000$ km s^{-1}. Clustering is clearly detected at low redshift: at $1.5 < z < 2.4$ in the 100 km s^{-1} bin we measure $\xi = 0.4 \pm 0.1$ for lines with $\log N_{HI} \geq 12.7$ cm^{-2}. The amplitude of the correlation at 100 km s^{-1} decreases significantly with increasing redshift from 0.4 ± 0.1 at $1.5 < z < 2.4$, to 0.14 ± 0.06 at $2.5 < z < 3.1$ and 0.09 ± 0.07 at $3.5 < z < 4.0$. A pattern of this type is predicted by the models of hierarchical formation of structures, in the interpretation, however, it should not be forgotten that a given column density corresponds to different overdensities at the various redshifts. In particular an absorber at $z = 2$ is dynamically analogous to an absorber that has column density several times higher at $z = 3$.

3.4 Voids and protoclusters

Voids, i.e. regions with a significant underdensity of absorption lines, are occasionally observed in QSO spectra (Dobrzycki & Bechtold 1991, Cristiani et al. 1997). The typical sizes observed so far are of the order of few tens comoving Mpc. Figure 8 shows two voids (of 54 and 43 Mpc) observed in the spectrum of the object HE2217-2818. The joint probability of finding two voids with a size larger than 40 comoving Mpc in a random distribution of lines at $z \sim 2$ is of the order of 2×10^{-4}. A third void of 61 Mpc is observed in the spec-

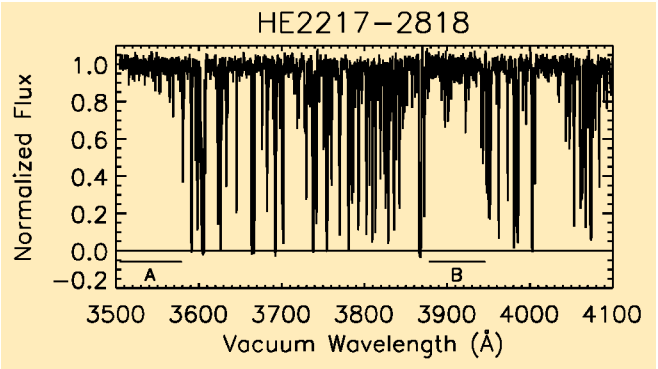

Figure 8: The spectrum of HE2217–2818 with two voids regions. The voids are indicated as A at z = 1.912 and B at z = 2.218.

trum of HE0515-44. There are different ways to produce a void in the forest: a large fluctuation in the gas density of the absorbers, an enhanced UV ionising radiation from nearby QSOs, feedback from forming galaxies or AGN heating the proto-cluster gas. In particular Theuns et al. (2000) have shown how a typical quasar sight-line intersects one protocluster per unit redshift. It is interesting to note that the void B in the spectrum of HE2217-2818 corresponds to a region of above-than-average Doppler parameter (see above), indicating that the gas in the void has been heated. To give a definitive answer about the nature of these voids, deep imaging and follow-up spectroscopy are needed, in order to identify possible AGN and/or galaxies at the redshift of the voids. This is a challenging programme but well within the possibilities of the VLT.

4. Acknowledgements

We are indebted to all people involved in the conception, construction and commissioning of UVES and UT2 for the quality of the data used in this paper, obtained in the first weeks of operation of the instrument.

References

Ballester P., Modigliani A., Boitquin O., Cristiani S., Hanuschik R., Kaufer A., Wolf S., 2000, *The Messenger*, **101**, 31.
Cristiani, S., D'Odorico, S., Fontana, A., Giallongo, E., Savaglio, S., 1995, MNRAS, 273, 1016
Cristiani, S., D'Odorico, S., D'Odorico, V., Fontana, A., Giallongo, E., Savaglio, S., 1997, *MNRAS*, **285**, 209.
Davé R., Hernquist L., Katz N., Weinberg D.H., 1999, *ApJ* **511**, 521.
Dekker, H., D'Odorico S., Kaufer A., Delabre B., Kotzlowski H., 2000, SPIE Proceedings 4008, 534.
Dobrzycki A., Bechtold J., 1991, *ApJ* **377**, L69.
Gunn J.E., Peterson B.A., 1965, *ApJ*, **142**, 1633.
Hu, E. M., Kim, T.-S., Cowie, L. L., Songaila, A., Rauch, M., 1995, *AJ*, **110**, 1526.
Hui L., Gnedin N. Y., 1997, *MNRAS*, **292**, 27.
Kim, T.-S., Hu, E.M., Cowie, L.L., Songaila, A., 1997, *AJ*, **114**, 1.
Kim T.-S., Cristiani S., D'Odorico S., 2000, *A&A* submitted.
Kirkman, D., Tytler, D., 1997, *AJ*, **484**, 672.
Kulkarni, V. P., Huang, K., Green, R. F., Bechtold, J., Welty, D.E., York, D.G., 1996, *MNRAS*, **279**, 197.
Lu, L., Sargent, W.L.W., Womble, D.S., Takada-Hidai, M., 1996, *ApJ*, **472**, 509.
Machacek M.E., Bryan G.L., Meiksin A., Anninos P., Thayer D., Norman M., Zhang Y., 2000, *ApJ* **532**, 118.
Rauch, M., Carswell, R.F., Chaffee, F.H., Foltz, C. B., Webb, J. K., Weymann, R. J., Bechtold, J., Green, R. F., 1992, ApJ, 390, 387.
Sargent, W. L. W., Young, P. J., Boksenberg A. Tytler, D., 1980, ApJS, 42, 41.
Schaye J., Theuns T., Rauch M., Efstathiou G., Sargent W.L.W., 2000, *MNRAS*, **318**, 817.
Steidel C.C., Pettini M., Adelberger K.L. astro-ph/0008283.
Theuns T., Mo H.J., Schaye J., astro-ph/0006065.
Weymann, R.J., et al., 1998, *ApJ*, **506**, 1.
Williger, G.M., Baldwin, J.A., Carswell, R.F., Cooke, A.J., Hazard, C., Irwin, M.J., McMahon, R.G., Storrie-Lombardi, L.J., 1994, *ApJ*, **428**, 574.

Email address: scristia@eso.org

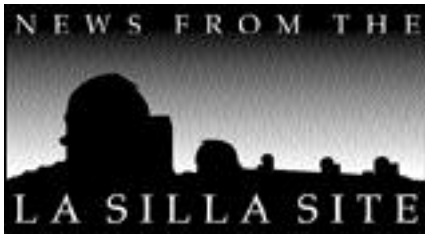

The La Silla New Page

2p2 Team News

H. JONES

Personnel Movements

In September we welcomed new team member Lisa Germany from Australia. Lisa is a new ESO Fellow and has interests in supernovae and their use in cosmological distance determinations.

September, however, was also a month for departures when we said goodbye to long-time team member James Brewer. James was a pivotal member of the 2p2 Team since his arrival at ESO in 1996. He has returned to Canada to take up a position at the University of British Columbia, in Vancouver, Canada. We wish him all the best under northern skies.

At the start of November, Rene Mendez formally took charge as Team Leader, replacing Patrick François, who will continue working with the team into early 2001.

First Stage of BOB-P2PP Software Installation at the ESO/MPG 2.2-m

The first commissioning period for the Broker for Observation Block (BOB) software at the ESO/MPG 2.2-m took place during October 7 to 16. This software will allow the 2.2-m to be controlled through observation blocks (OBs) in the same way as the VLT, 3.6-m and NTT telescopes. Thanks to the hard efforts of Tatiana Paz, Cristian Urrutia and Eduardo Robledo (of the La Silla Software and Communications Team), the several months of software writing in the lead-up to its first-test at the telescope paid off. During the October test nights it was possible to move the telescope around the sky and execute sequences of short test exposures, using OBs.

Much work is needed to refine and test the code in the coming months, particularly in the way it communicates between the telescope, CCD controller and image acquisition software. Thus, part of the challenge lies in coordinating the separate tasks of these systems, which may be called upon many times during a single sequence.

Additional technical time in November and December will be used to complete the development and testing. In the meantime, a new Instrument Package containing WFI-specific templates for use in P2PP is undergoing revision and testing.

Sub-Arcsecond Images with the Wide-Field Imager

On the night of October 19–20, the Wide-Field Imager (WFI) was producing 20-minute B-band exposures of 0.6 arcsec seeing. This impressive result demonstrates the significant gains that the recent work of Alain Gilliotte and Gerardo Ihle on the 2.2-m image quality have made. In the past, the 2.2-m has exhibited occasional astigmatism under certain pointing conditions (2p2 Team Report, *The Messenger* No. 100). However, recent improvements to the fixed points on which the M1 mirror sits by the opto-mechanical teams on La Silla, have diminished these effects. However, careful focus control is essential to take full advantage of these improvements.

On the same night, the WFI delivered 1.2-arcsec images at an airmass of 1.8, and closely followed the seeing measured by the DIMM seeing monitor.

Telescope Information

Remember to consult the 2p2 Team Web pages when you require any information about the ESO 1.52-m, Danish 1.54-m or ESO/MPG 2.2-m telescopes. These are regularly updated with recent news postings and information for new observers. They can be visited at http://www.ls.eso.org/lasilla/Telescopes/2p2T/ .